



ORIGINAL RESEARCH ARTICLE

Effect of Coherent Twin Boundary on the Low-Cycle Fatigue Property of 321 Austenitic Stainless Steel

Gang Xu, Jiexin Wu, Weiguo Wang, Yanyun Zhao, and Shuang Xia

Submitted: 2 November 2023 / Revised: 27 April 2024 / Accepted: 9 May 2024

In this work, the coherent component of twin boundaries (TBs) in AISI 321 austenitic stainless steel (SS) via grain boundary engineering (GBE) is statistically measured by the method of grain boundary inter-connection (GBIC) which is a parameter describing the grain boundary character intrinsically, and the influence of coherent TBs on the low-cycle fatigue property at 623 K is investigated. The GBIC results show that the content of $\{111\}$ GBICs which is the coherent component in $\Sigma 3$ boundaries is increased via GBE treatment. The fatigue investigation reveals that coherent TBs of a high fraction eliminate the cyclic softening phenomenon in 321 austenitic stainless steel, which results in a progressive strengthening effect in the process of cyclic loading. Microstructural analysis demonstrates coherent TBs effectively improve fatigue crack propagation resistance as they can restrain the growth of small cracks. It is evidenced that enhancing the length fraction of coherent TBs via GBE is feasible to controlling fatigue crack propagation for AISI 321SS.

Keywords 321 austenitic stainless steel, coherent twin boundary, fatigue crack, grain boundary engineering, grain boundary inter-connection

1. Introduction

AISI 321 is a titanium-stabilized austenitic stainless steel (SS) that is widely utilized in both the chemical and nuclear industries for its exceptional high-temperature mechanical properties and corrosion resistance (Ref 1, 2). It is commonly used to make structural components of a nuclear reactor, due to its advantageous characteristics in these environments. In real-world service conditions, the tubes experience cyclic loads resulting from operational adjustments. These loads induce periodic plastic deformation, leading to localized cyclic plastic damage in the material.

The microstructure (such as the deformed induced martensite, dislocation, grain boundary (GB), grain size, and other second phase precipitates) has an important effect on the fatigue crack growth rate and their corresponding path (Ref 3). GBs play important roles in the deflection/branching, path and local propagation rate of fatigue cracks during deformation of the materials under the fatigue load (Ref 4). The percolative phenomena in fatigue occur along some preferential GBs and often cause a serious material problem under different service environments (Ref 5).

Gang Xu, Jiexin Wu, and Weiguo Wang, School of Materials Science and Engineering, Fujian University of Technology, Fuzhou 350118, China; **Yanyun Zhao**, College of Nuclear Equipment and Nuclear Engineering, Yantai University, Yantai 264005 Shandong, China; and **Shuang Xia**, School of Materials Science and Engineering, Shanghai University, Shanghai 200444, China. Contact e-mails: wang_weiguo@vip.163.com and zhaoyanyun@ytu.edu.cn.

It was reported that the random high angle grain boundaries (RHAGBs) often become the preferential sites for the nucleation and propagation of fatigue cracks in copper during cyclic plastic deformation (Ref 6). Generally, RHAGBs do not permit penetration of slip/shear bands from grain to grain; hence, these defects can even pile up and accumulate to a high density at RHAGBs, inducing fatigue cracks. Sangid et al. (Ref 7, 8) reported that twin boundaries (TBs) (i.e., $\Sigma 3$ boundaries) have lower static interfacial energy and provide a stronger barrier to dislocation slip transmission compared to other low Σ coincidence site lattice (CSL) GBs in 310SS. This leads to a greater degree of dislocation pile-up at $\Sigma 3$ GBs than at other low Σ CSL GBs, potentially enhancing the mechanical properties of the material. However, the authors (Ref 7) also observed that when dislocation pile-up within a grain at $\Sigma 3$ GBs is substantial, a portion of the dislocations can cross the boundary and continue to move within another grain. This ability of $\Sigma 3$ GBs to mitigate strain concentration and reduce the likelihood of crack nucleation at these boundaries enhances the fracture toughness of the materials. Kobayashi et al. (Ref 9) found that the ratio of intergranular fracture segments to the total crack length was lower for the 304SS specimen with the higher fraction of low Σ CSL special boundaries (SBs) which were introduced via grain boundary engineering (GBE). Recently, Guan et al. (Ref 10) investigated that the low-cycle fatigue life of Cu-16 at.% Al alloys is distinctly improved by means of GBE. As such, GBE is an effective way to enhance the fatigue performance of face-centered cubic (FCC) metals for improving the fatigue performance of FCC metals with low-to-medium stacking fault energy. Kobayashi et al. (Ref 11) reported that the growth rate of fatigue cracks at coherent TBs was clearly lower than that at RHAGBs and the introduction of higher length fraction of coherent TBs leads to a lower contribution of intergranular fracture to total crack length and a lower local propagation rate of fatigue crack in AISI 304SS.

It must be noted that the traditional GBE characterizes the TBs primarily based on the GB misorientation, which involves only three independent parameters, usually the axis/angle pair, such as $\langle u v w \rangle / \theta$. Here, u , v , and w represent the Miller indices defining the rotation axis, and θ indicates the rotation angle between the adjacent grains. Notably, only two of the three parameters of the rotation axis $\langle u v w \rangle$ are independent ones. However, this method is very difficult to make a classified statistics concerning the coherent and non-coherent components of the TBs because the characterization of a GB needs five parameters (The misorientation in angle-axis pair contains three parameters as mentioned above, GB normal orientation in the crystallographic frame gives another two), i.e., the GB interconnection (GBIC) which is a parameter describing the GB character intrinsically (Ref 12-14). For example, all $\Sigma 3$ boundaries in FCC metals have the same misorientation of $\langle 111 \rangle / 60^\circ$, but they may have the GBICs of $\{111\} / \{111\}$ (coherent component) and $\{111\} / \{115\}$ or $\{011\} / \{011\}$ and so on (non-coherent component). The structure and performance of the coherent $\Sigma 3$ boundaries are quite different compared to that of the non-coherent ones (Ref 15). Nevertheless, the traditional GBE researches hardly consider the GBICs of the $\Sigma 3$ boundaries in FCC metals as there is no effective analysis method of GBIC.

Since coherent $\Sigma 3$ boundary has an important effect on improving the fatigue property of FCC metals (Ref 11), it is very necessary to make a classified statistics concerning the coherent component of the $\Sigma 3$ boundaries in FCC metals of GBE processed. Recently, the method of quantitative GBIC measurement with statistical significance (Ref 16) has been established based on the early developed five parameters analysis (FPA) (Ref 17, 18). Therefore, in the present work, we will analyze the coherent components of TBs in AISI 321SS via GBE and investigate the influence of coherent TBs on the low-cycle fatigue (LCF) property. It is expected to help us understand the influence of the coherent $\Sigma 3$ boundaries (i.e., coherent TBs) on the LCF property.

2. Material and Methods

2.1 Materials

The austenitic stainless steel utilized in this study was commercial-grade AISI 321SS. The chemical composition of this steel, expressed as weight percentages, consisted of 0.013 C, 17.46 Cr, 9.04 Ni, 1.443 Mn, 0.094 Mo, 0.177 Ti, 0.712 Si, 0.027 P, and 0.005 S, with Fe comprising the remainder. To improve the non-uniform microstructure of commercial-grade AISI 321SS, a solid solution treatment was performed at 1373 K for 60 min, followed by water quenching to room temperature (RT). The solution-treated specimens underwent unidirectional multi-pass rolling with a thickness reduction of 50% at RT, followed by annealing in a furnace at 1373 K for 30 min. This cold-rolling process with 50% thickness reduction was repeated once more. The cold-rolled samples were divided into two parts. One part was annealed at 1323 K for 40 min followed by water quenching, which was termed and denoted as non-GBE in this paper. The other part was subjected to annealing at 1323 K for 5 min and then quenched into water as the starting material for the subsequent GBE treatment. The GBE sample was obtained by rolling deformation of 4%

thickness reduction at RT and then annealed at 1323 K for 20 min followed by water quenching. Both of two parts of samples were annealed at 1173 K for 2 h to stabilize carbon as TiC by titanium to prevent chromium carbide precipitation.

2.2 The Fatigue Testing

The specimens utilized in this work for fatigue testing were flat-sheets with a thickness of 2.5 mm. The specimens were prepared following ISO 12106 guidelines, with their lengthwise direction aligned parallel to the rolling direction of the plate. The dimensions of the specimens are shown in Fig. 1. The fatigue tests were performed in air under uniaxial strain-controlled conditions using an MTS electro-hydraulic servo fatigue testing facility. The strain range was set at $\pm 0.3\%$, and a triangular waveform with a frequency of 0.25 Hz was applied. Additionally, a strain ratio of $R = -1$ was employed. During the fatigue testing process, the test temperature was carefully maintained at 623 ± 2 K which is the design temperature as the components of a VVER reactor work in temperature range of 564-594 K (Ref 2). Before the fatigue testing, the tensile properties are determined by tensile testing of the small GBE and non-GBE specimens at 623 K to estimate the fatigue strain amplitude. The tensile properties (average values) are shown in Table 1.

2.3 The Microstructure Analysis

The samples were obtained using electric discharge wire cutting device and subsequently underwent mechanical polishing. Afterward, electrolytic polishing was performed using a solution of $\text{HClO}_4:\text{C}_2\text{H}_5\text{OH}$ in a 1:9 volume ratio for two min, with a polishing voltage of 30 V and a current of approximately 0.5 A. The samples were mounted in a FEI Nova NanoSEM 450 field emission scanning electron microscope (FE-SEM) coupled with an Oxford Aztec facility for electron backscatter diffraction (EBSD) mapping. During the EBSD data acquisition, the operating parameters were selected as an acceleration voltage of 20 kV, a spot size of 4.5, a working distance of 10 mm and a step size of 2 μm .

2.4 Grain Boundary Filtration and GBIC Determination

To probe the specific characteristics of $\Sigma 3$ boundaries in the samples, the single-section FPA proposed by Rohrer et al. (Ref 17, 18) was employed. The data collection process involved evaluating multiple regions of the sample surface using EBSD, ensuring a minimum of 50,000 GB measurements per sample. This meticulous approach ensures that the resulting data are both accurate and representative. According to actual need, the

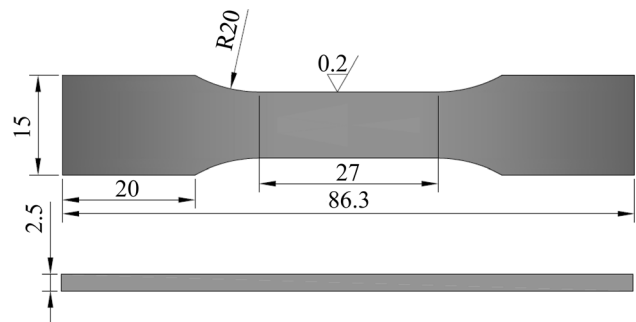


Fig. 1 The dimensions of the fatigue samples. (units: mm)

Table 1 Tensile properties of AISI 321SS at 623 K

	$\sigma_{0.2}$, MPa	σ_b , MPa	δ , %
Non-GBE	171	379	55
GBE	163	389	61

$\sigma_{0.2}$: yield strength; σ_b : tensile strength; δ : elongation.

EBSD raw data were processed into varied format such as orientation imaging microscopy (OIM) and GB character distribution (GBCD).

The extracted grain boundaries were subsequently categorized into distinct groups based on their misorientation characteristics, specifically utilizing the rotation axis and angle pair notation $\langle u \ v \ w \rangle / \theta$. For $\sum 3$ GB, the fixed misorientation is $\langle 1 \ 1 \ 1 \rangle / 60^\circ$. The acquired boundary data underwent rigorous axis filtering and angular filtering procedures to further ensure its accuracy. Initially, a fixed rotation axis $\langle 1 \ 1 \ 1 \rangle$, characterized by a low Miller index and a deviation angle of $\pm 8^\circ$, was selected. Subsequently, the GBs associated with this fixed rotation axis were subjected to further filtering using a rotation angle deviation of $\pm 2.5^\circ$. This is much more rigorous than Brandon (Ref 19) and Aust-Palumbo (Ref 20) criteria. This rigorous filtering process ensured that only GBs with a fixed misorientation were considered for subsequent analysis. After axis filtration, the grain boundaries with the same rotation axis were further filtered according to the rotation angles ($\theta = 60^\circ$).

The GBs that passed the filtering process with fixed misorientation were subsequently analyzed using FPA to determine the distribution of grain boundary planes (GBPD). Furthermore, the GBIC method proposed by Wang (Ref 21-23) was employed to identify the presence of $\{1 \ 1 \ 1\} / \{1 \ 1 \ 1\}$ GBIC information. Equations 1 and 2, where $(h_1 \ k_1 \ l_1)$ and $(h_2 \ k_2 \ l_2)$ are the inter-connected planes at the boundaries and $R_{[u \ v \ w] / \theta}$ is the misorientation matrix relevant to the given misorientation $[u \ v \ w] / \theta$, were utilized for calculation and determination. It is important to note that u , v , and w are normalized results, where $u^2 + v^2 + w^2 = 1$. Additionally, $(h_1 \ k_1 \ l_1)$ denotes a location point with a high GBPD orientation strength which was represented by a parameter of multiple of random distribution (MRD) and the MRD value needs to reach 1.10 or more, while $(h_2 \ k_2 \ l_2)$ can be calculated using Eq 1. If $(h_2 \ k_2 \ l_2)$ also represents a location point with a relatively strong orientation strength in the fixed misorientation GBPD (MRD ≥ 1.10), it can be inferred that a GB interface match exists between $(h_1 \ k_1 \ l_1)$ and $(h_2 \ k_2 \ l_2)$.

$$\begin{bmatrix} h_2 \\ k_2 \\ l_2 \end{bmatrix} = R_{[uvw] / \theta} \begin{bmatrix} h_1 \\ k_1 \\ l_1 \end{bmatrix} \quad (\text{Eq 1})$$

$$R_{[uvw] / \theta} = \begin{bmatrix} u^2(1 - \cos \theta) + \cos \theta & uv(1 - \cos \theta) - w \cos \theta & uw(1 - \cos \theta) + v \sin \theta \\ uv(1 - \cos \theta) + w \sin \theta & v^2(1 - \cos \theta) + \cos \theta & vw(1 - \cos \theta) - u \sin \theta \\ uw(1 - \cos \theta) - v \sin \theta & vw(1 - \cos \theta) + u \sin \theta & w^2(1 - \cos \theta) + \cos \theta \end{bmatrix} \quad (\text{Eq 2})$$

Equation 3 is employed to evaluate the length fraction of GB that exhibits a fixed orientation deviation. This fraction is derived from the filtering process applied to the GB information.

$$F = AP + B(PM/W) \quad (\text{Eq 3})$$

In this computational analysis, the fitting parameters $A = 0.4888$ and $B = 0.0393$ are incorporated (Ref 24). These parameters are used in Eq 3 (Ref 16), where P is the length fraction of the GBs (out of the entire GBs), M is the MRD value of the intensity peak positions corresponding to the considered GBIC which is determined on the base of the GBPD map, W is the full width at half maximum (FWHM) of the weighted Gaussian misorientation distribution curve for the GBs, and F is the length fraction of the GBs with the considered GBIC.

The determination of the proportion of coherent TBs, as obtained from the aforementioned approach, is founded on the principles of stereology and statistical analysis. However, in order to further ascertain the nature of a specific GB being a coherent twin boundary (TB), this research incorporates Wright's (Ref 25) overlapping pole figure method to characterize and analyze the $\sum 3$ boundaries possessing $\{1 \ 1 \ 1\} / \{1 \ 1 \ 1\}$ GBIC features. Particularly, if the $\{1 \ 1 \ 1\}$ overlapping pole figures of the two adjacent grains on both sides of GB display a coincident $\{1 \ 1 \ 1\}$ pole point and the normal direction of GB trace passes through this coincident pole point, the boundary is classified as a coherent TB. For the detailed description of GBIC determination, it is recommended to refer to (Ref 16).

3. Results and Discussion

3.1 Initial Microstructural Characteristics

Figure 2(a) and (b) illustrates orientation imaging microscopy (OIM) of AISI 321SS before and after GBE. The average grain size was found to be similar between the Non-GBE and GBE samples, measuring $24.4 \mu\text{m}$ and $24.5 \mu\text{m}$, respectively. The grain orientations in the non-GBE specimens were randomly distributed, indicating the absence of texture formation. In contrast, the grain orientations in the GBE specimens exhibited a tendency toward $\{0 \ 1 \ 1\} / \text{ND}$ (ND is the normal direction of the plate), causing the gradual emergence of a slight texture during the GBE process. Figure 2(c) and (d) shows GBCD micrographs obtained by TPA method. Notably, it was found that the length fraction of $\sum 3$ -related ($\sum = 3^n$) CSL boundaries significantly increases from 40.2 to 77.1% after undergoing the GBE process.

Figure 3 gives the GBPDs and the weighted Gaussian misorientation distributions (GBPD) of the $\sum 3$ boundaries for the AISI 321SS samples (GBE and non-GBE). Table 2 summarizes the detailed information for the $\sum 3$ boundaries reconstructed and extracted based on the OIMs of samples as processed. The specific data are provided in Table 2. We can

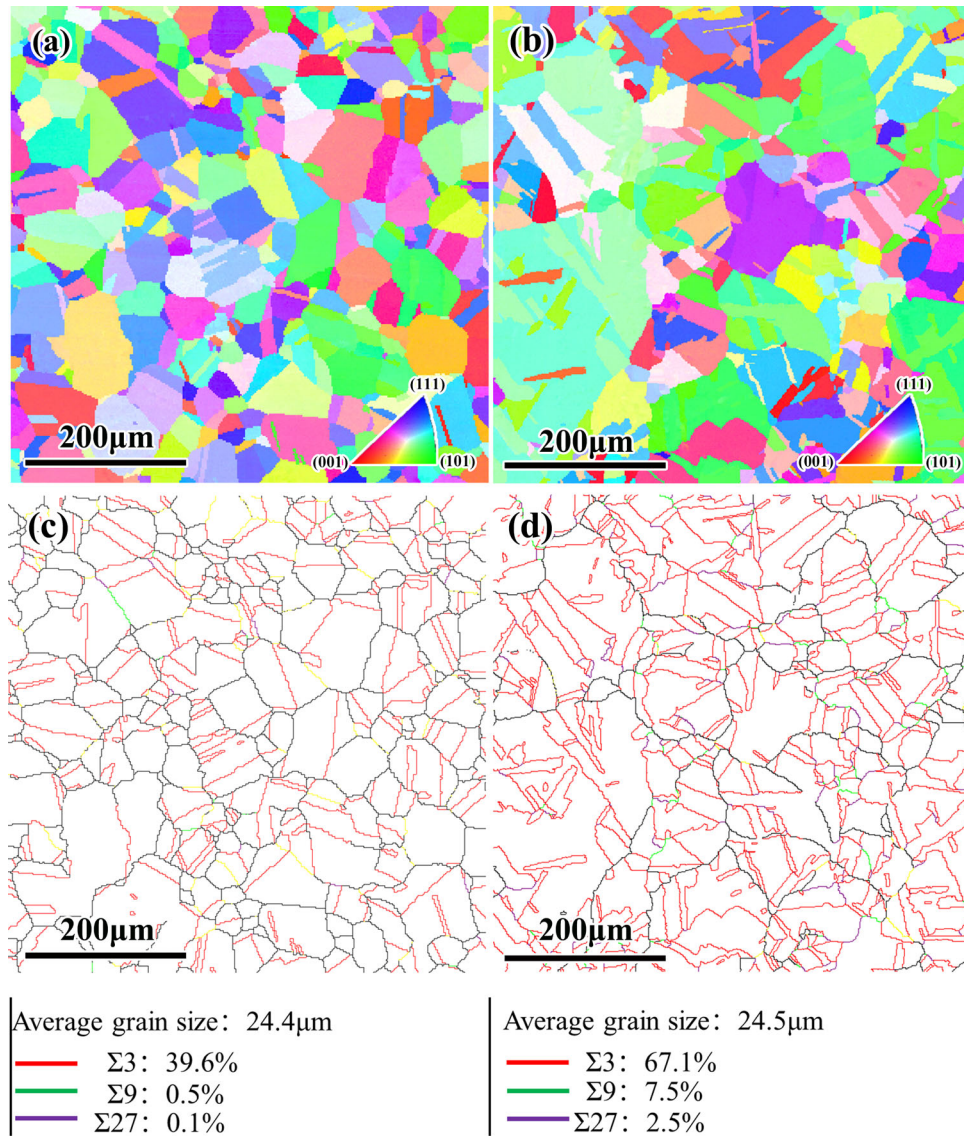


Fig. 2 GB characterized micrographs with the data of the OIM (a), (b), and GBCD (c), (d) for non-GBE and GBE AISI 321SS

see the $\Sigma 3$ boundary planes are exclusively distributed on $\{1\ 1\ 1\}$ which has the maximum intensity in Fig. 2(a) and (b). The GB planes of the $\Sigma 3$ boundaries demonstrate a preferential relative to the $\{1\ 1\ 1\}$ crystal planes. Figure 3(c) and (d) illustrates the W values for the $\Sigma 3$ boundaries with the fixed $\langle 1\ 1\ 1 \rangle / 60^\circ$ misorientation in the GBE and non-GBE samples, respectively. The GBE sample exhibits an MRD value of 6.95, while the non-GBE sample has an MRD value of 3.47. This demonstrates that there are more $\Sigma 3$ boundary planes exclusively distributed on $\{1\ 1\ 1\}$ in the GBE samples than that in the non-GBE ones.

Table 2 summarizes the detailed information for the $\Sigma 3$ boundaries reconstructed and extracted based on the OIMs of samples as processed. It is found that the length fraction of the coherent $\Sigma 3$ boundaries out of entire GBs in GBE sample is 48.5% which is two times higher than that (23.6%) in the non-GBE one (Fig. 4). The non-GBE sample exhibits 59.5% fraction of coherent $\Sigma 3$ boundaries among the $\Sigma 3$ boundaries. With the proportion of $\Sigma 3$ boundaries increasing from 39.6 to 67.1%, this fraction rise to 72.3% in the GBE sample. The

cause should be that the transformation from incoherent $\Sigma 3$ boundaries to coherent ones occurred during twin growth (Ref 21).

3.2 Fatigue Test Results

Figure 5 illustrates the cyclic stress response (CSR) of both the non-GBE and GBE samples. It demonstrates that the fatigue life of the non-GBE sample is 33727 cycles, while the fatigue life of the GBE sample is increased by 64% to 55142 cycle. It is worth noting that the CSR curves of the samples present significant divergence, indicating a substantial decrease in tensile stress amplitude with increasing coherent TBs. For non-GBE samples, the material exhibits initial cyclic hardening, followed by cyclic softening, a brief cyclic saturation, and then secondary hardening before a rapid stress drop. This four-stage cyclic stress evolution at low strain amplitudes is characteristic of solution annealed austenitic steels (Ref 26). The initial hardening primarily results from increased dislocation multiplication due to applied deformation. Interactions between dislocations, as well as between dislocation and solute atoms

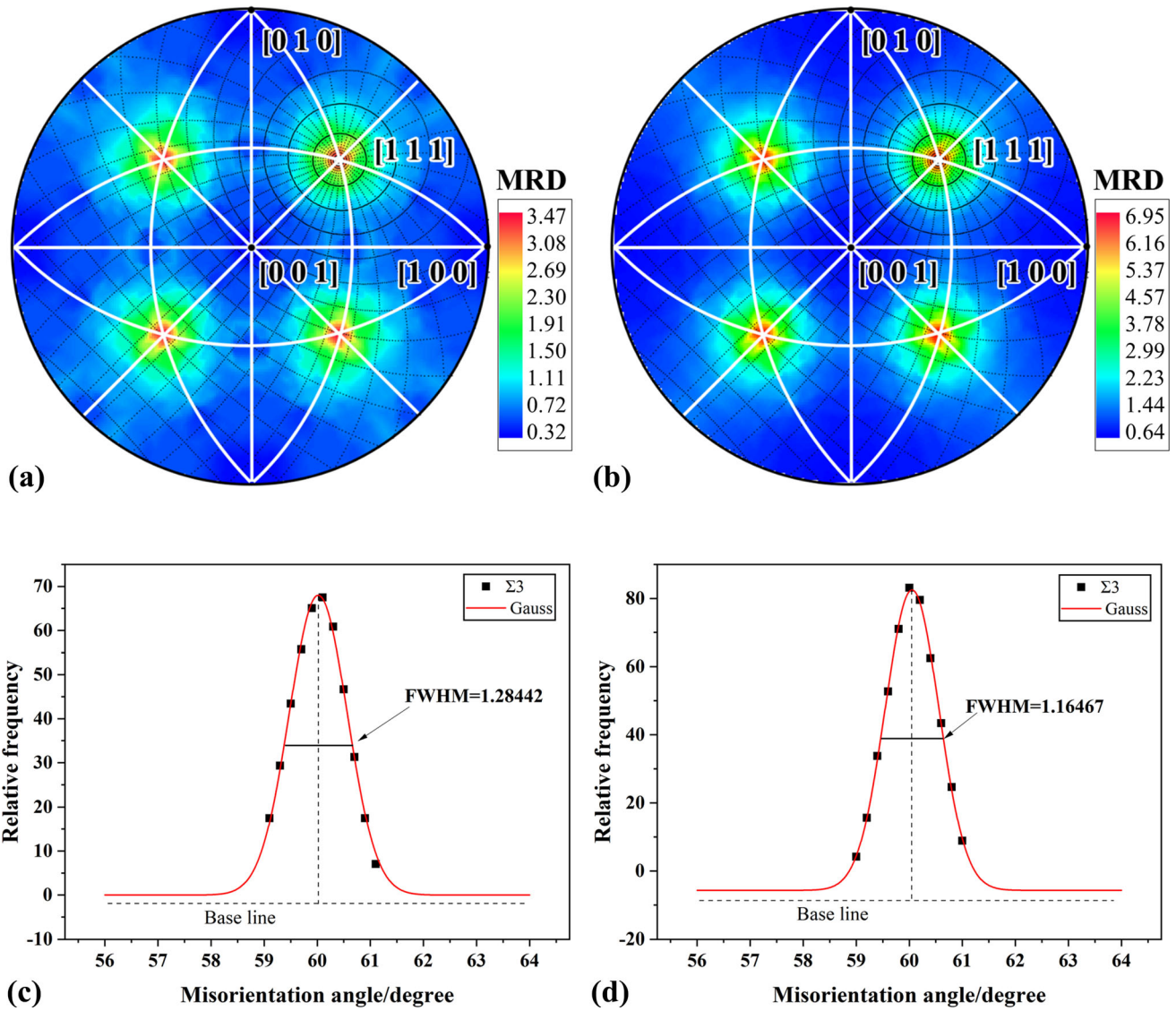


Fig. 3 The orientation distribution of $\langle 111 \rangle / 60^\circ$ GBs and full width at half maximum of GBIC in AISI 321SS. (a) and (c), non-GBE sample; (b) and (d) GBE sample

Table 2 The specific interface matching of GBs in AISI 321SS

	GBIC	$P, \%$	M	$W, -$	$F, \%$
Non-GBE	$\{111\}/\{111\}$	39.6	3.47	1.28442	23.6
GBE	$\{111\}/\{111\}$	67.1	6.95	1.16467	48.5

increase material strength. The subsequent cyclic softening occurs as the annihilation rate of dislocations surpasses their multiplication rate, reducing dislocation density. As cycling continues, dislocation structures rearrange, increasing the average free path of dislocations. Eventually, dislocation multiplication and annihilation reach equilibrium, leading to a brief saturation before the onset of secondary hardening. The secondary hardening phase is characterized in materials like 316 (Ref 27) and 304 (Ref 28) stainless steels by the formation of planar slip bands, comprising dislocation dipoles, multipolar

configurations, and loops, as well as an increase in strain-induced martensitic transformations.

In contrast, the GBE specimen demonstrates a continuous cyclic hardening behavior that persists until fatigue fracture. Notably, throughout this entire process of continuous cyclic hardening, the maximum peak stress attained remains lower than the maximum tensile stress exhibited by the non-GBE sample after experiencing cyclic softening.

In-depth analysis reveals a discernible disparity in the apex tensile stress and the initial cycle's stress amplitude in AISI 321SS both before and after the GBE treatment. Specifically, the non-GBE specimen exhibits a maximum cyclic hardening amplitude of 37 MPa, while post-GBE treatment, this value increases to 38.8 MPa, indicating a comparable amplitude. However, the position of maximum peak stress diverges in both instances. The non-GBE specimen reaches its maximum peak stress at the 81st cycle, while the GBE sample does not reach this point until the 50,536th cycle. These findings suggest that GBE treatment considerably diminishes the cyclic hardening rate of AISI 321SS. During the fatigue process, the generation

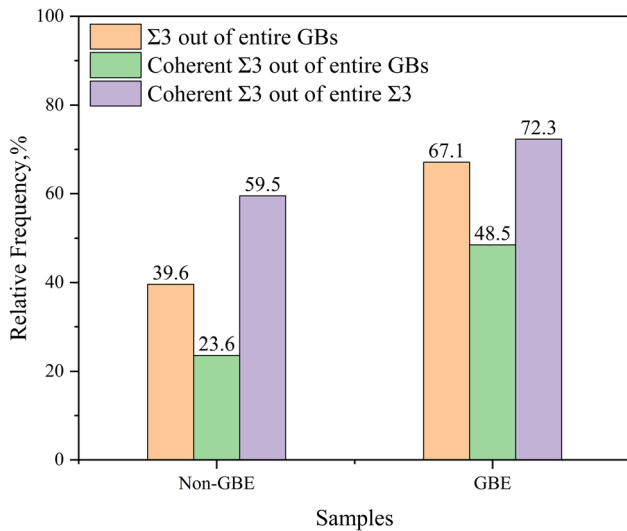


Fig. 4 Length fractions of the $\Sigma 3$ boundaries in non-GBE and GBE sample

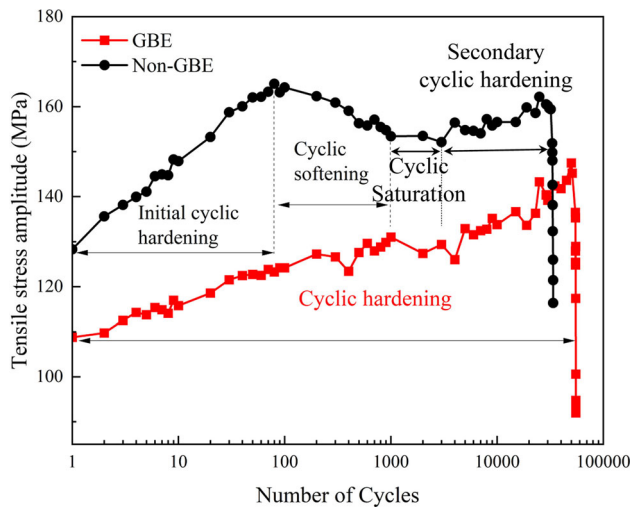


Fig. 5 The cyclic stress response curves of the for non-GBE and GBE AISI 321SS at 623 K

of dislocations and their interactions act to enable the material to adjust to the imposed cyclic strain amplitude. Cyclic hardening during fatigue primarily results from the proliferation, accumulation, and interaction of these dislocations, as well as the dynamic strain aging (DSA) effect triggered by cyclic loading stress. In the deformation process of face-centered cubic

FCC) metals with medium to low stacking fault energy, the degree of dislocation pile-up at the RHAGBs is higher than that at the $\Sigma 3$ GBs, and when the degree of dislocation pile-up at the $\Sigma 3$ GBs is significant, a portion of the piled-up dislocations traverse the $\Sigma 3$ GBs to continue gliding (Ref 7, 10). Accordingly, we conclude that the inclusion of coherent $\Sigma 3$ boundaries in GBE samples enhances the activated dislocation slip routes and reduces the strain resistance of the material induced by fatigue strain, thereby accounting for the observed decrease in cyclic hardening rate.

The deformation hysteresis curve for the first and half-life cycles is illustrated in Fig. 6. As Fig. 5 indicates, the non-GBE

specimen reaches the cyclic saturation stage at half-life, thereby attaining a dynamic equilibrium in relation to microstructural changes under cyclic loading. In contrast, the GBE specimen continues to demonstrate cyclic hardening beyond its half-life. The emergence of DSA (Ref 29), indicated by the stress oscillations in the hysteresis curve, is noticeable in the first cycle and plays a pivotal role in the initial cyclic hardening. It is believed that the DSA effect of austenitic stainless steel in the initial stage mainly caused by the Suzuki atmospheres of solute atoms forming in faulted areas of partial dislocations (Ref 30). As the cycle count increases from the first cycle to the half-life, the serration amplitude of the hysteresis curve diminishes, and the DSA effect in the GBE sample vanishes entirely.

As the DSA is an intriguing interaction that occurs between dislocations and solute species during cyclic deformation (Ref 26), the attenuation in the DSA effect during the saturation stage in the non-GBE sample is attributed to a higher degree of dislocation cross-slip activity. In other words, screw dislocations can easily cross-slip to escape from solute atom atmospheres (Ref 31).

The complete lack of DSA effects in the GBE samples may be ascribed to a relatively stable state of dislocation multiplication and annihilation during the half-life stage. It is reported that the interfacial energies of coherent $\Sigma 3$ boundaries (i.e., coherent TBs) are the lowest among all the GBs (Ref 31, 32). The lowest interfacial energy and the smallest lattice distortion will induce more moving dislocations to slip across coherent $\Sigma 3$ boundaries (Ref 33, 34) and thus weaken the interaction between dislocations and solute species. Therefore, it should be the reason for the complete absence of DSA effects that the coherent TBs of a high fraction induced by GBE.

3.3 Fracture Surface Characteristics

The fatigue fracture morphologies of both the non-GBE and GBE samples are depicted in Fig. 7. The non-GBE sample fracture exhibits a characteristic river pattern, while the presence of ratchet marks suggests the formation of multiple crack sources on the sample's surface, as depicted in Fig. 7(a). In contrast, the fatigue fracture of the GBE sample features a beach pattern, as shown in Fig. 7(b). The emergence of the beach pattern in the GBE sample implies that the GBE process enhanced the toughness of the AISI 321SS, as the occurrence of beach patterns is frequently associated with high toughness materials. In brittle materials, these beach patterns tend to be erased due to cyclic compressive stress (Ref 35). The source area of the relatively flat fatigue crack is also seen to undergo a notable increase after the implementation of GBE treatment, indicating that a greater number of cycles are required for the initiation of fatigue cracks.

The character and structure of GBs play an important role in impeding slip within the material. Mughrabi et al. (Ref 36) suggested that the inherent causes of fatigue crack initiation are closely related to the localization of cyclic strain and the irreversibility of dislocation slip. Li et al. (Ref 6) found that low- Σ CSL GBs exhibit inherently higher fatigue cracking resistance compared to other GBs. It has been reported that GBs with lower static interfacial energy offer a stronger barrier against crack nucleation at GBs (Ref 37). Kobayashi et al. (Ref 38) have found that low- Σ CSL boundaries demonstrate greater resistance to fatigue crack nucleation compared to random boundaries. Zhang et al. (Ref 39) and Li et al. (Ref 40, 41) pointed out that the fatigue-resistance ability of TBs is better

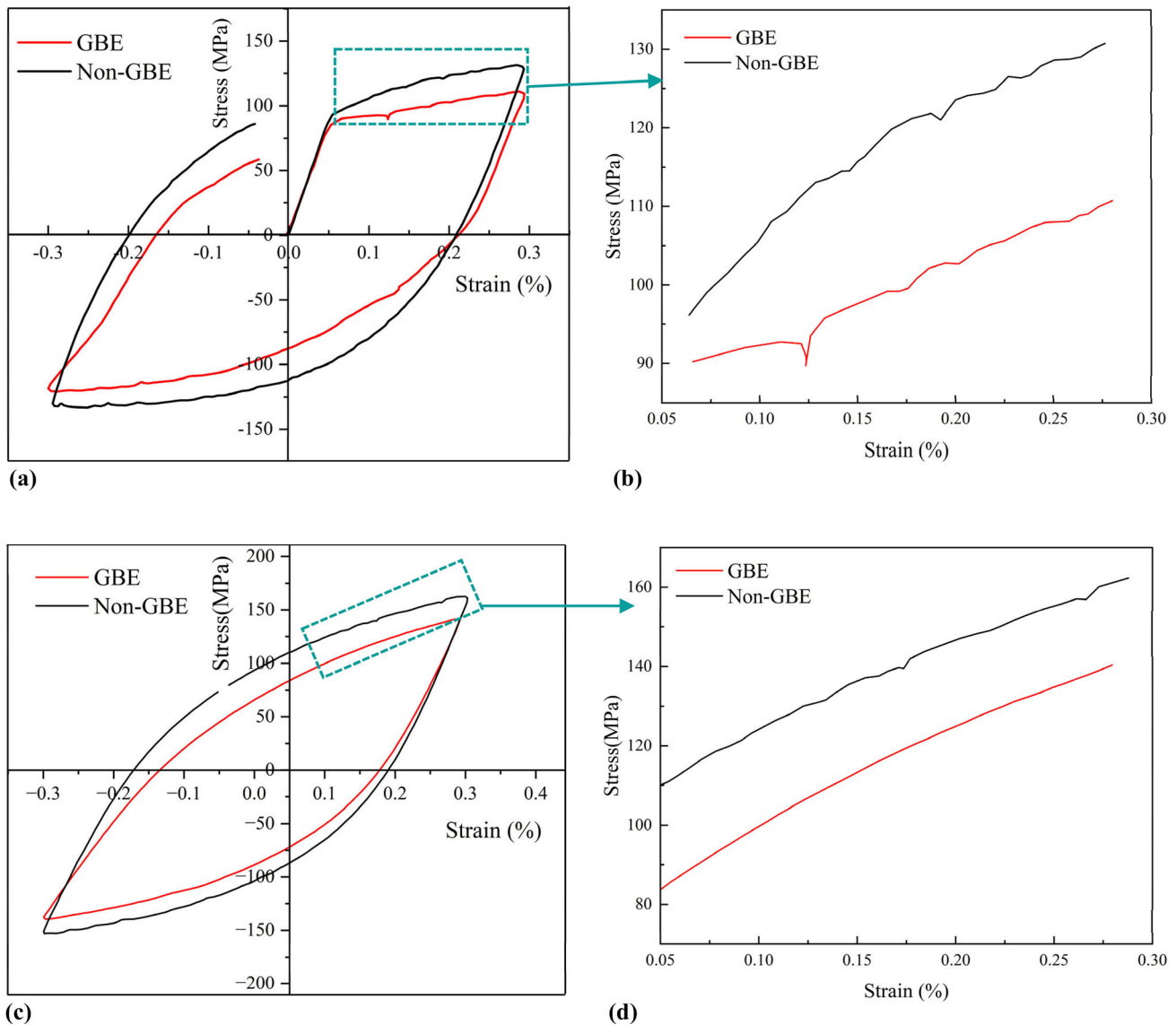


Fig. 6 The hysteresis loop curves of AISI 321SS at 623 K. (a) and (c) the hysteresis loop in the 1st cycle and half-life cycle, (b) and (d) serrations in a tensile portion of a hysteresis loop in (a) and (c)

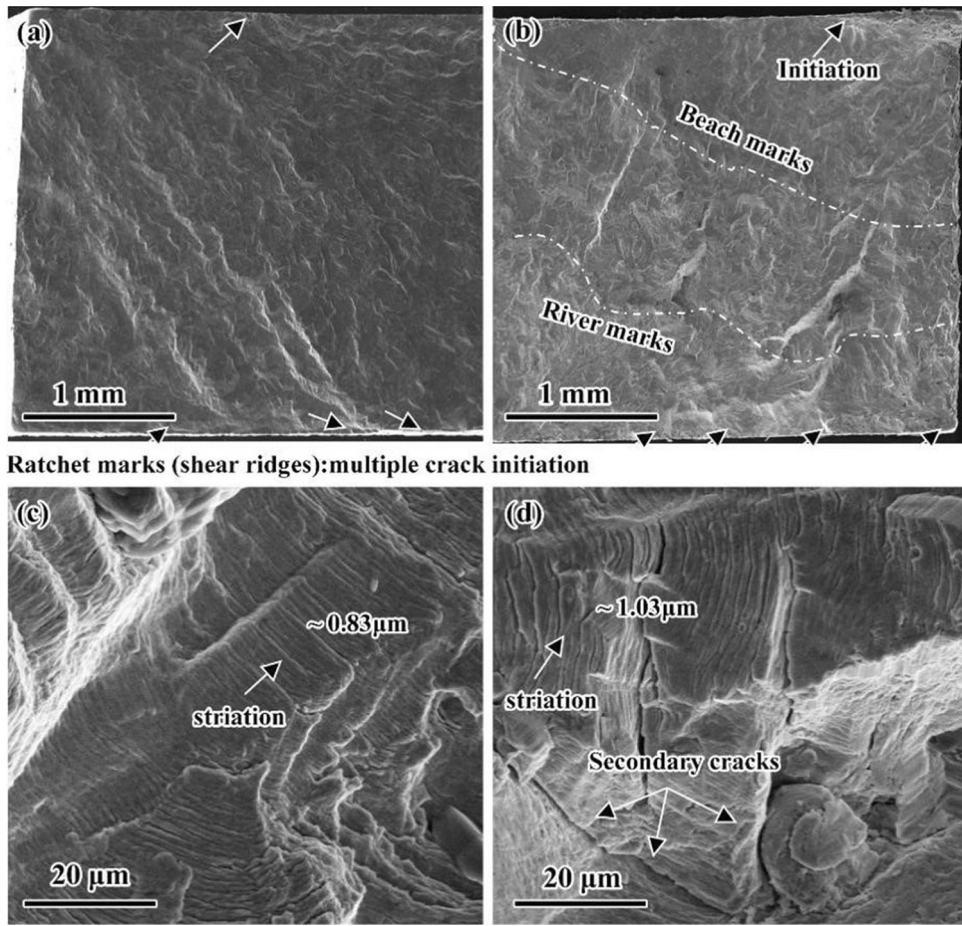
than that of RHAGBs to some extent in low-cycle fatigue tests. Therefore, it is suggested that the increase in coherent $\Sigma 3$ GBs suppresses the accumulation of dislocations and the localized strain during cyclic loading in the fatigue crack initiation stage. As a result, the fatigue crack initiation life of the material is effectively improved.

The fatigue crack propagation morphology, marked by the presence of striations, is illustrated in Fig. 7(c) and (d). In the non-GBE sample, the fatigue crack propagation appears relatively even, stemming from planar slip during the fatigue process. Figure 7(c) shows that the striations have a width of approximately $0.83 \mu\text{m}$, while the striations increase to approximately $1.03 \mu\text{m}$ in the GBE samples, as shown in Fig. 7(d), which can be ascribed to the strength decrease induced by increase of the coherent TBs fraction. Along the propagation path of the primary crack in GBE sample, multiple secondary cracks can be detected, which can be attributed to the encounter between the stress concentration region at the crack tip and the coherent TBs during the propagation of the primary

crack. Due to the lower level of critical stress required for crack propagation along coherent TBs compared to that required for propagation along the primary crack direction, a greater number of secondary cracks form there. The presence of these secondary cracks facilitates the relief of stress at the tip of the primary crack. Therefore, a higher number of fatigue cycles is necessary for crack propagation in the area of primary stress. This phenomenon provides a plausible explanation for the remarkable improvement in the fatigue life of the GBE specimen, despite the occurrence of larger crack growth within a single cycle. Nonetheless, to assess the validity of the hypothesis, further investigation into the propagation of secondary cracks is discussed in subsequent sections.

3.4 Microcracks in the Gauge Section

Figure 8 illustrates the fatigue crack growth behavior in both the non-GBE and GBE samples. In comparing the two samples, a distinctive tendency for crack growth can be observed. The fatigue crack in the non-GBE sample exhibits a tortuous path,



Ratchet marks (shear ridges):multiple crack initiation

Fig. 7 The fracture surface of non-GBE (a) and GBE (b) samples. (c) and (d) the cracks growth areas in non-GBE (a) and GBE (b) samples

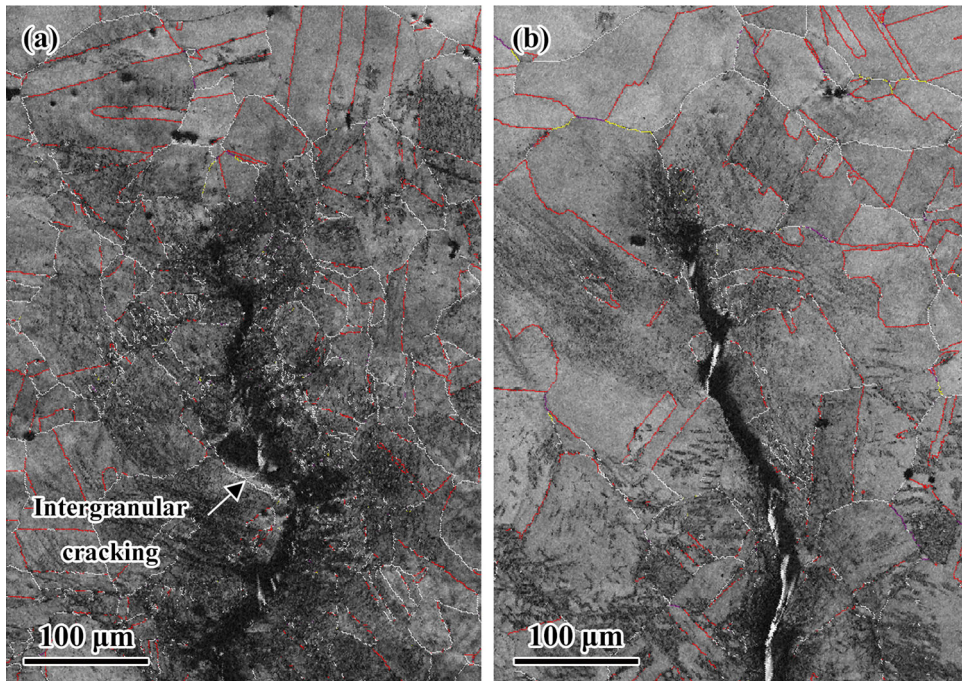


Fig. 8 The fatigue crack propagation morphology observed by the EBSD. (a) the non-GBE sample; (b) the GBE sample

accompanied by the occurrence of intergranular cracks along the route of crack growth. Additionally, signs of accumulating plastic deformations are observed in the grain structure surrounding the crack, as manifested by the presence of black slip lines. In contrast, the crack propagation path in the GBE sample appears smoother, indicating transgranular fracture resulting from the increased prevalence of coherent TBs. Moreover, the GBE sample demonstrates a considerable reduction in the presence of black slip marks near the crack compared to the non-GBE sample. This suggests that the coherent TBs of a high fraction induced by GBE effectively impede the accumulation of plastic strain and localized cyclic strain.

Due to the high residual stress and severe lattice distortion around the main crack, the EBSD calibration efficiency remains low, making it difficult to accurately calibrate the interface orientation around the crack. However, a small fatigue crack with lower residual stress was found in the opposite position (frontal position) relative to the main crack of the GBE sample. The OIM map of this crack is shown in Fig. 9(a). We can see the GBE sample exhibits a typical transgranular fatigue crack.

During the main crack propagation process in the GBE sample, the appearance of multiple secondary microcracks can be observed. Figure 9(b), (c) (d) and (e) shows the representation of some fatigue cracks in the GBE sample in the band contrast (BC) map with GBCD. The four regions outlined by white dashed boxes in the figure indicate where the cracks

stopped propagating at the edge of the coherent $\Sigma 3$ GBs. Specifically, the crack in region 1 stopped propagating at the $\Sigma 3$ GB, the crack in region 2 stopped propagating at the $\Sigma 3$ - $\Sigma 3$ - $\Sigma 9$ triple junction, while the cracks in regions 3 and 4 both stopped at the $\Sigma 3$ GBs. However, to further confirm a specific GB as a coherent TB, this research incorporates Wright's overlapping pole figure method to characterize and analyze the $\Sigma 3$ boundaries possessing $\{111\}/\{111\}$ GBIC features. Through a detailed analysis using the Wright method, it was found that all the microcracks in these regions stopped at the coherent TBs. Additionally, the occurrence of crack termination at RHAGBs was rare, which indicates that coherent TBs play a valuable role in inhibiting the propagation of fatigue cracks.

Krupp (Ref 42) suggested that small crack propagation was determined by the spatial arrangement of the slip plane corresponding to the local stress direction. Once a certain stress on the slip plane is reached, plastic deformation by dislocation occurs. However, when the crack tip reaches the GB, plastic deformation is constrained, leading to a reduced number of small cracks. The coherent TB, despite its inherent "resistance" effect in inhibiting crack propagation along the crack path, can still be penetrated by cracks along the main crack. This phenomenon could be attributed to the inclined orientation of the coherent TB on the main crack in the loading direction, compounded by additional stress and unique dislocation of the slip. These factors result in the concentration of

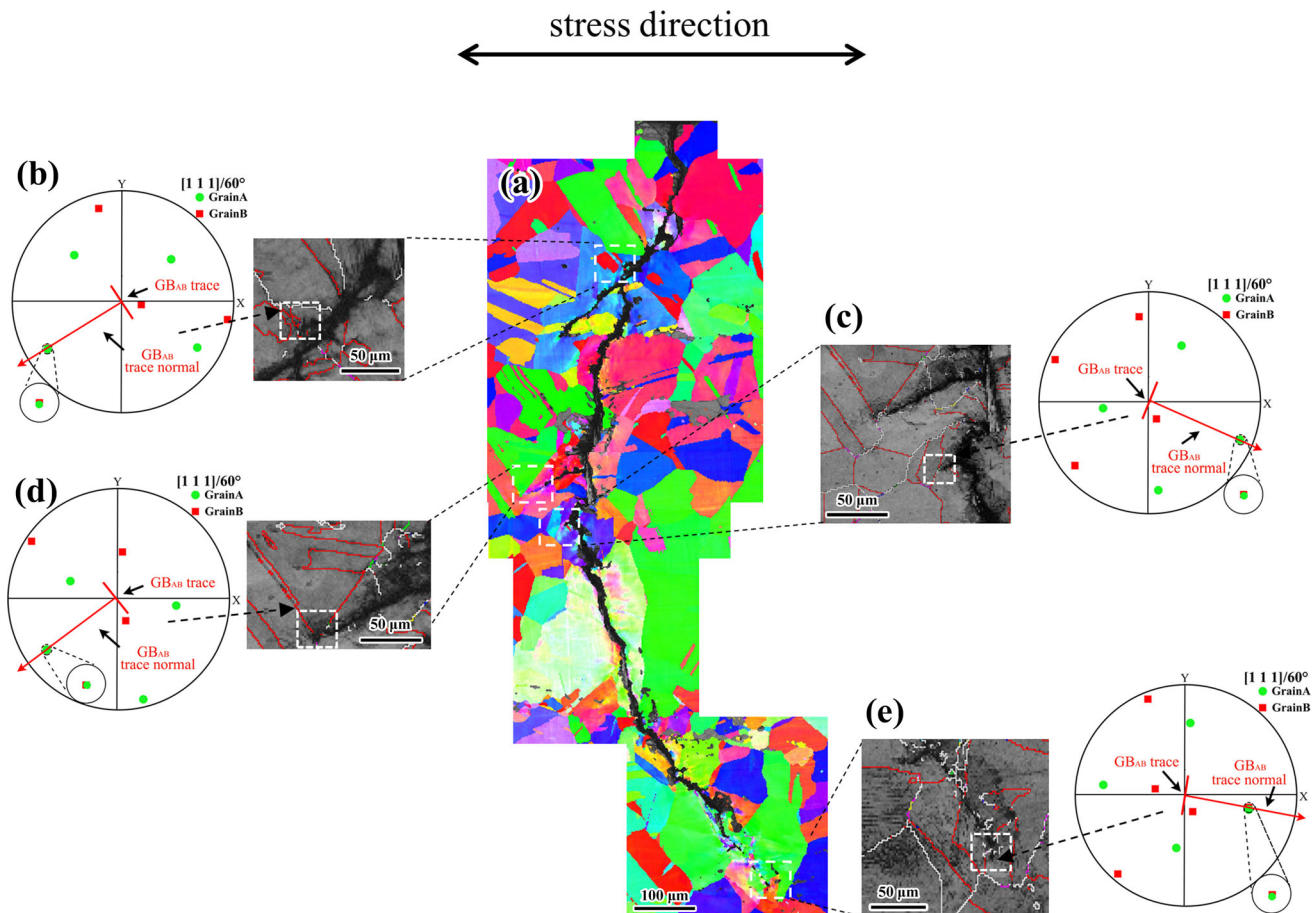


Fig. 9 The OIM map of the crack in the GBE sample, as well as the BC + GBCD map of the crack tip microregion and the analysis of overlapping pole figure GB traces

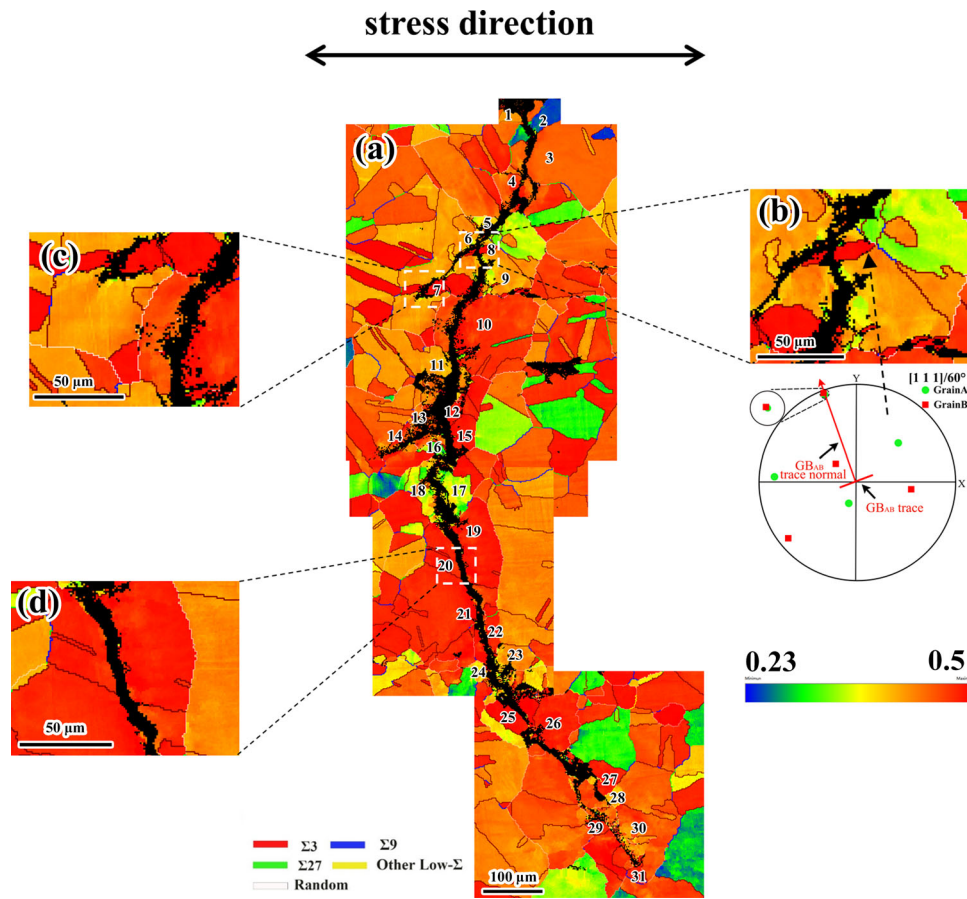


Fig. 10 The distribution of Schmid factors in the GBE sample.

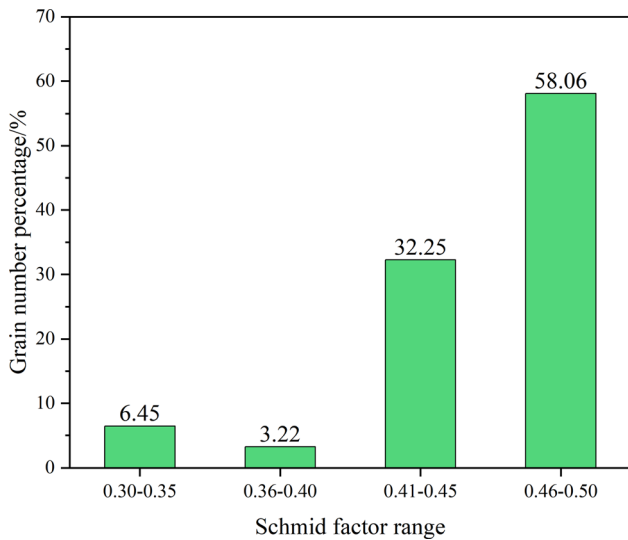


Fig. 11 Schmid factor distribution graph around the crack.

the slip band near the coherent TB, thereby guiding the fatigue crack to penetrate the coherent TB. However, the fatigue crack propagation process is influenced by other factors such as the Schmid factor (SF).

Figure 10 depicts the distribution of SF for cracks in the GBE sample. The SF calculated in the figure represents the maximum values for each grain, and the numbered grains on

the figure are all on the crack path. The figure illustrates 31 grains (including the main crack and branch cracks) on the crack path, where the range of SFs for “cracking across grain” (CAG) is 0.3-0.5. Figure 11 delineates the distribution of SFs for cracking across grain in the GBE sample, categorized into four ranges of 0.30-0.35, 0.36-0.40, 0.41-0.45, and 0.46-0.50 based on their SF values.

As the SF increases, so the strength of the material decreases. Activation of multiple slip systems occurs when SF ranges from 0.355 to 0.425, while only one slip system is activated when SF exceeds 0.425 (Ref 37). In this study, crack propagation predominantly occurs in grains with higher SF values (0.46-0.50), suggesting that during fatigue only one slip system is primarily active. Grains with lower SF values, referred to as hard-oriented grains, exhibit greater resistance to slip initiation, resulting in hindered crack propagation, and subsequently leading to significant crack deflection and branching. Conversely, grains with higher SF values, known as soft-oriented grains, facilitate easier slip initiation, hence exhibiting lower resistance to crack propagation inhibition. As a result, cracks tend to penetrate grains with higher SF values, and the depth of cracks increases with the number of grains penetrated.

As depicted in Fig. 10, most of the propagation of the main crack occurs directly through the grains. When the crack penetrates grains with SF = 0.3 (grain 2) and SF = 0.31 (grain 16), a significant deflection occurs post-penetration. Upon examining the propagation path of the main crack, it is evident

that the crack favors extending through grains with higher SF values (0.46-0.50).

Grains with higher SF values generally exhibit lower fatigue crack resistance due to increased stress concentration, which makes them more susceptible to crack penetration. It can also be seen from Fig. 10 that the crack first penetrates the grain with SF = 0.5 (grain 7), and upon doing so, the fatigue crack deflects and stops at the coherent TB. Similarly, when the crack penetrates a grain with SF = 0.5 (grain 8) flanked by coherent TBs, the crack exhibits a branching phenomenon, underscoring the role of coherent TBs in resisting crack propagation. Furthermore, the presence of coherent TBs may guide the path for deviations caused by fatigue crack propagation, thereby preventing or slowing down the crack expansion.

Based on the above analysis, coherent $\Sigma 3$ boundaries which possess orderly and stable arrangement of crystal lattices are more effective in inhibiting fatigue crack propagation compared to other GBs. Although some cracks may still penetrate coherent TBs, their development is often characterized by deflection and branching, which reduces the probability of fatigue cracks propagation and extends the service life of the materials. Accordingly, it can be concluded that enhancing the proportion of coherent TBs should be a feasible path to improve the LCF life of AISI 321SS.

4. Conclusion

In the present work, the GBIC method is employed to analyze the coherent components of $\Sigma 3$ boundaries (i.e., TBs) in AISI 321SS treated via GBE and the influence of coherent TBs on the strain-controlled LCF property is investigated. The following conclusions can be drawn.

1. In AISI 321 SS, there are coherent and non-coherent TBs, denoted as $\{1\ 1\ 1\}/\{1\ 1\ 1\}$ and non $\{1\ 1\ 1\}/\{1\ 1\ 1\}$ GBICs, respectively. Following GBE treatment, the length fraction of TBs and the content of coherent component in TBs are both increased considerably.
2. Coherent TBs of a high fraction induced by GBE can provide more slip possibilities in AISI 321SS, hindering the cyclic strain localization and resulting in a shift toward continuous cyclic hardening behavior in the cyclic stress response. The presence of coherent TBs effectively inhibits the expansion of these secondary cracks, leading to reduced stress concentration and improved fatigue crack propagation resistance. Therefore, increasing the fraction of coherent TBs via GBE can be a feasible path to improve the LCF property for AISI 321SS.

Acknowledgments

This work was supported by the National Key Research and Development Program of China with grant No.2018YFE0122100), Fujian Province Ningde City “Public Recruitment of Leading Talents” Key Core Technology Research and Development Program of Ningde City in Fujian Province with grant No.ND2023J001, the Development Plan of Shandong Province Young Innovation Team of Higher Education Institutions with

grant No.2022KJ273, and Fujian University of Technology Talent Construction Fund with grant No. E0600465.

Data availability

Data will be made available on request.

Conflict of interest

The authors declare that they have no known competing financial interests or personal relationships that could have appeared to influence the work reported in this paper.

Reference

1. M.D. Manfrinato, L.S. de Almeida, L.S. Rossino, A.M. Kliauga, L. Melo-Máximo, D.V. Melo-Máximo, and R.C. Morón, Scratch Testing of Plasma Nitrided and Nitrocarburized AISI 321 Steel: INFLUENCE of the Treatment Temperature, *Mater. Lett.*, 2022, **317**, 132083
2. S.S. Kasana and O.P. Pandey, Effect of Heat Treatment on Microstructure and Mechanical properties of Boron Containing Ti-Stabilized AISI-321 Steel for Nuclear Power Plant Application, *Mater. Today Commun.*, 2021, **26**, 101959
3. S. Suresh and R.O. Ritchie, Propagation of Short Fatigue Cracks, *Int. Met. Rev.*, 1984, **29**(1), p 445–475.
4. S. Kobayashi, A. Kamata, and T. Watanabe, A Mechanism of Grain Growth-Assisted Intergranular Fatigue Fracture in Electrodeposited Nanocrystalline Nickel-Phosphorus Alloy, *Acta Mater.*, 2015, **91**, p 70–82.
5. T. Watanabe, The Impact of Grain Boundary Character Distribution on Fracture in Polycrystals, *Mater. Sci. Eng. A*, 1994, **176**(1–2), p 39–49.
6. L.L. Li, Z.J. Zhang, and P. Zhang, Higher Fatigue Cracking Resistance of Twin Boundaries than Grain Boundaries in Cu Bicrystals, *Scr. Mater.*, 2011, **65**(6), p 505–508.
7. M.D. Sangid, T. Ezaz, H. Sehitoglu, and I.M. Robertson, Energy of Slip Transmission and Nucleation at Grain Boundaries, *Acta Mater.*, 2011, **59**(1), p 283–296.
8. M.D. Sangid, H.J. Maier, and H. Sehitoglu, The Role of Grain Boundaries on Fatigue Crack Initiation-An Energy Approach, *Int. J. Plast.*, 2011, **27**(5), p 801–821.
9. S. Kobayashi, M. Nakamura, S. Tsurekawa, and T. Watanabe, Effect of Grain Boundary Microstructure on Fatigue Crack Propagation in Austenitic Stainless Steel, *J. Mater. Sci.*, 2011, **46**, p 4254–4260.
10. X.J. Guan, Z.P. Jia, S.M. Liang, F. Shi, and X.W. Li, A Pathway to Improve low-Cycle Fatigue Life of Face-Centered Cubic Metals via Grain Boundary Engineering, *J. Mater. Sci. Technol.*, 2022, **113**, p 82–89.
11. S. Kobayashi, M. Hirata, S. Tsurekawa, and T. Watanabe, Grain Boundary Engineering for Control of Fatigue Crack Propagation in Austenitic Stainless Steel, *Procedia Eng.*, 2011, **10**, p 112–117.
12. W. Wang, Y. Cui, G.S. Rohrer, C. Cai, S. Chen, X. Gu, and Y. Lin, Grain Boundary Inter-Connections of $\Sigma 5$ Boundaries in a High Purity Iron with a Uniform Microstructure, *Scr. Mater.*, 2019, **170**, p 62–66.
13. D.N. Dunn, G.J. Shiflet, and R. Hull, Quantitative Three-Dimensional Reconstruction of Geometrically Complex Structures with Nanoscale Resolution, *Rev. Sci. Instrum.*, 2002, **73**, p 312–330.
14. A.D. Rollett, S.B. Lee, R. Campman, and G.S. Rohrer, Three-Dimensional Characterization of Microstructure by Electron Back-Scatter Diffraction, *Annu. Rev. Mater. Res.*, 2007, **37**, p 627–658.
15. A. Du, W. Wang, X. Gu, S. Chen, Y. Cui, Y. Lin, and L. Hong, The Dependence of Precipitate Morphology on the Grain Boundary Types in an Aged Al-Cu Binary Alloy, *J. Mater. Sci.*, 2021, **56**, p 781–791.
16. X. Yang, W. Wang, and X. Gu, The Near Singular Boundaries in BCC Iron, *Philos. Mag.*, 2022, **102**(5), p 440–466.
17. G.S. Rohrer, D.M. Saylor, B.E.L. Dasher, B.L. Adams, A.D. Rollett, and P. Wynblatt, The Distribution of Internal Interfaces in Polycrystals, *Int. J. Mater. Res.*, 2021, **95**(4), p 197–214.
18. D.M. Saylor, B.S. El-Dasher, B.L. Adams, and G.S. Rohrer, Measuring the Five-Parameter Grain-Boundary Distribution from Observations of Planar Sections, *Metall. Mater. Trans. A*, 2004, **35**, p 1981–1989.

19. D.G. Brandon, The Structure of High-Angle Grain Boundaries, *Acta Metall.*, 1966, **14**(11), p 1479–1484.
20. G. Palumbo, K.T. Aust, E.M. Lehockey, U. Erb, and P. Lin, On a More Restrictive Geometric Criterion for “Special” CSL Grain Boundaries, *Scr. Mater.*, 1998, **38**(11), p 1685–1690.
21. W. Wang, Y. Dai, J. Li, and B. Liu, An Atomic-Level Mechanism of Annealing Twinning in Copper Observed by Molecular Dynamics Simulation, *Cryst. Growth Des.*, 2011, **11**(7), p 2928–2934.
22. F. Abdeljawad, P. Lu, N. Argibay, B.G. Clark, B.L. Boyce, and S.M. Foiles, Grain Boundary Segregation in Immiscible Nanocrystalline Alloys, *Acta Mater.*, 2017, **126**, p 528–539.
23. W.G. Wang, C.H. Cai, G.S. Rohrer, X.F. Gu, Y. Lin, S. Chen, and P.Q. Dai, Grain Boundary Inter-Connections in Polycrystalline Aluminum with Random Orientation, *Mater Charact.*, 2018, **144**, p 411–423.
24. W.G. Wang, A.H. Du, X.M. Yang, S. Chen, and Y. Lin, The Method for Quantitative Characterization of Grain Boundary Inter-Connections, Chinese Patent No.202011173146.8
25. S.I. Wright and R.J. Larsen, Extracting Twins from Orientation Imaging Microscopy Scan Data, *J. Microsc.*, 2002, **205**(3), p 245–252.
26. G.P. Reddy, P. Dinesh, R. Sandhya, K. Laha, and T. Jayakumar, Behavior of 321 Stainless Steel under Engineering Stress and Strain Controlled Fatigue, *Int. J. Fatigue*, 2016, **92**, p 272–280.
27. M.S. Pham and S.R. Holdsworth, Dynamic Strain Ageing of AISI 316L During Cyclic Loading at 300°C: Mechanism, Evolution, and its Effects, *Mater. Sci. Eng. A*, 2012, **556**, p 122–133.
28. Y.Y. Cui, W.T. Wang, H. Wang, B. Li, P. Zhao, and F.Z. Xuan, Cyclic Behavior and Damage Mechanism of 304 Austenitic Stainless Steel under Different Control Modes, *J. Mater. Res. Technol.*, 2024, **30**, p 854–865.
29. W.H. Yang, P.M. Cheng, Y. Li, R. Wang, G. Liu, L. Xin, J.Y. Zhang, D.P. Li, H.B. Zhang, and J. Sun, Dynamic Strain Aging-Mediated Temperature Dependence of Ratcheting Behavior in a 316LN Austenitic Stainless Steel, *Mater. Sci. Eng. A*, 2023, **862**, 144503
30. M.S. Pham and S.R. Holdsworth, Dynamic Strain Ageing of AISI 316L During Cyclic Loading at 300 C: Mechanism, Evolution, and its Effects, *Mater. Sci. Eng. A*, 2012, **556**, p 122–133.
31. L. Lu, Y. Shen, X. Chen, L. Qian, and K. Lu, Ultrahigh Strength and High Electrical Conductivity in Copper, *Sci.*, 2004, **304**(5669), p 422–426.
32. N. Shibata, F. Oba, and T. Yamamoto, Structure, Energy and Solute Segregation Behaviour of [110] Symmetric Tilt Grain Boundaries in Yttria-Stabilized Cubic Zirconia, *Philos. Mag.*, 2004, **84**(23), p 2381–2415.
33. L.L. Li, Z.J. Zhang, P. Zhang, Z.G. Wang, and Z.F. Zhang, Controllable Fatigue Cracking Mechanisms of Copper Bicrystals with a Coherent Twin Boundary, *Nat. Commun.*, 2014, **5**(1), p 3536.
34. Z. Shen, R.H. Wagoner, and W.A.T. Clark, Dislocation and Grain Boundary Interactions in Metals, *Acta Metall.*, 1988, **36**(12), p 3231–3242.
35. N.W. Sachs and J. Fail, Understanding the Surface Features of Fatigue Fractures: How they Describe the Failure Cause and the Failure History, *Anal. Prev.*, 2005, **5**(2), p 11–15.
36. H. Mughrabi, Microstructural Fatigue Mechanisms: Cyclic Slip Irreversibility, Crack Initiation, Non-linear Elastic Damage Analysis, *Int. J. Fatigue*, 2013, **57**, p 2–8.
37. A. Das, Grain Boundary Engineering: Fatigue Fracture, *Philos. Mag.*, 2017, **97**(11), p 867–916.
38. S. Kobayashi, T. Inomata, H. Kobayashi, S. Tsunekawa, and T. Watanabe, Effects of Grain Boundary- and Triple Junction-Character on Intergranular Fatigue Crack Nucleation in Polycrystalline Aluminum, *J. Mater. Sci.*, 2008, **43**(11), p 3792–2799.
39. Z.J. Zhang, P. Zhang, L.L. Li, and Z.F. Zhang, Fatigue Cracking at Twin Boundaries: Effects of Crystallographic Orientation and Stacking Fault Energy, *Acta Mater.*, 2012, **60**(6–7), p 3113–3127.
40. L.L. Li, P. Zhang, Z.J. Zhang, and Z.F. Zhang, Effect of Crystallographic Orientation and Grain Boundary Character on Fatigue Cracking behaviors of Coaxial Copper Bicrystals, *Acta Mater.*, 2013, **61**(2), p 425–438.
41. L.L. Li, Z.J. Zhang, P. Zhang, J.B. Yang, and Z.F. Zhang, Difference in Fatigue Cracking Behaviors of Cu Bicrystals with the Same Component Grains but Different Twin Boundaries, *Scr. Mater.*, 2015, **95**, p 19–22.
42. U. Krupp, Fatigue Crack Propagation in Metals and Alloys: Microstructural Aspects and Modelling Concepts, *Mater. Today*, 2007, **10**, p 53.

Publisher's Note Springer Nature remains neutral with regard to jurisdictional claims in published maps and institutional affiliations.

Springer Nature or its licensor (e.g. a society or other partner) holds exclusive rights to this article under a publishing agreement with the author(s) or other rightsholder(s); author self-archiving of the accepted manuscript version of this article is solely governed by the terms of such publishing agreement and applicable law.